Journal of Materials Chemistry A

Accepted Manuscript

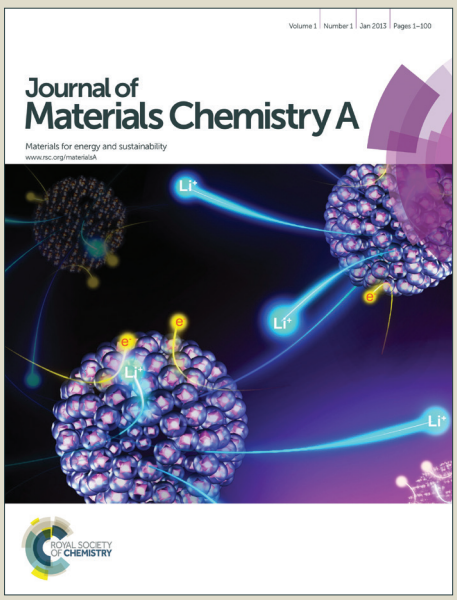

ROYAL SOCIETY OF CHEMISTRY

www.rsc.org/materialsA

Journal Name

ARTICLE

Reduced Graphene Oxide Grafted by Polymer of Polybromopyrroles to Nanocomposites with Superior Performance for Supercapacitors

Received 00th January 20xx,
Accepted 00th January 20xx

DOI: 10.1039/x0xx00000x

www.rsc.org/

Shouzhi Wang, Ligang Gai*, Haihui Jiang, Zhenzhen Guo, Nana Bai, and Jianhua Zhou

An integrated structure has been designed by grafting polymer of polybromopyrroles (PPBP) onto reduced graphene oxide (RGO) to produce RGO/PPBP nanocomposites with superior electrochemical performance for supercapacitors. The RGO/PPBP nanocomposites are featured with high nitrogen content (> 9 at.%), enhanced degree of graphitization, improved specific surface area, abundant micropores, and a tunable hierarchical structure on the basis of sample characterizations with XRD, Raman, FT-IR, XPS, SEM, high-resolution TEM, BET, and scanning probe microscopy (SPM) techniques. The grafting of PPBP onto RGO not only suppresses agglomeration and restacking of RGO but also tailors the growth of PPBP on RGO, producing a developed hierarchical structure beneficial for mass/charge transfer. The synergistic effect between RGO and PPBP ensures superior electrochemical performance of RGO/PPBP. In a three-electrode mode, the typical RGO/PPBP electrode presents a galvanostatic capacitance (C_g) of 256 F g^{-1} at a current density of 10 A g^{-1}, with capacitance retention of 99.2% after 10,000 cycles in 1 mol L^{-1} H_2SO_4. More significantly, the typical RGO/PPBP‖RGO/PPBP supercapacitor cell exhibits a high C_g value of 272 F g^{-1} at 5 A g^{-1}, with capacitance retention of 91.9% after 10,000 cycles. Also, relatively high energy density values of 13.6, 9.4, and 6.7 Wh kg^{-1} with corresponding power density of 0.5, 2.5, and 10 kW kg^{-1} are achieved, enabling the tested cell to stay at the high level for carbon-based supercapacitors with aqueous electrolyte.

1. Introduction

Supercapacitors have attracted increasing interest in the electrochemical energy conversion/storage systems because they can deliver high power density and extremely long cycle life and complement or even replace batteries in the energy storage field, especially when high power delivery or uptake is needed.[1] In recent years, graphene has been considered a promising candidate as a supercapacitor electrode material due to its attractive characteristics such as large specific surface area (S_{BET}), good flexibility, excellent electrical conductivity, good thermal and chemical stability, extended potential window, and abundant surface functional groups.[2,3] However, the capacitance of supercapacitors based on individual graphene or reduced graphene oxide (RGO) is usually limited by the easy agglomeration and restacking of graphene sheets, leaving behind intersheet pores that are not sufficient for accessibility to the electrolyte.[3-8]

To enhance the electrochemical performance of graphene-based supercapacitors, many approaches have been developed: (i) creating large S_{BET} and/or tuning pore size distribution (PSD) through chemical activation of graphene or exfoliated graphite oxide;[8,9] (ii) introducing spacers to suppress restacking of graphene sheets;[10,11] (iii) designing corrugated or three-dimensional (3D) graphene;[12,13] (iv) doping sp^2 carbon with heteroatoms to modulate the electronic structure and increase the wettability of graphene;[14-16] and (v) constructing graphene-based nanocomposites to maximize the synergistic effect between the components.[1-3,17,18] For construction of graphene- and RGO-based nanocomposites, graphene oxide (GO) obtained through chemical exfoliation of graphite is universally employed as a matrix to tailor the growth of electroactive species that, in turn, hinder restacking of the sheets.[18] This is because the functional oxygen-containing groups on GO sheets can serve as nucleation sites to anchor foreign species.[19] Meanwhile, GO is reduced to graphene or RGO in chemical or thermal conditions, resulting in the formation of graphene- or RGO-based nanocomposites. Moreover, the graphene or RGO matrix not only improves the

[a] Institute of Advanced Energy Materials and Chemistry, School of Chemistry and Pharmaceutical Engineering, Qilu University of Technology, Jinan 250353, People's Republic of China.
[b] *Corresponding author. E-mail: liganggai@qlu.edu.cn

† Electronic Supplementary Information (ESI) available: Synthesis of GO and PBPs, SEM images of RGO, PPBP, and the electrode film, SPM images of RGO/PPBP-2, and additional characterization data. See DOI: 10.1039/x0xx00000x

electrical conductivity of the composites but also buffers the volume change of electroactive species in electrodes during cycling.[18]

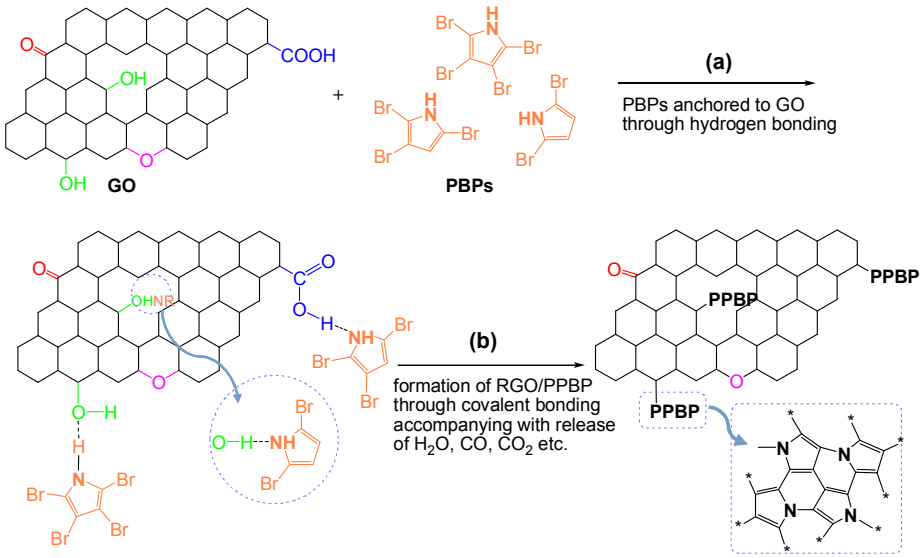

Scheme 1. Illustration of the formation mechanism of RGO/PPBP nanocomposite. For simplicity, the C=C bonds in GO and RGO are omitted.

Recently, we have reported on a new type of polymer with hierarchical architecture and crystalline CN_x ($x \leq 0.25$) domains through deep thermal cyclodebromination of polybromopyrroles (PBPs).[20] This new-type polymer exhibits high volumetric capacitance and specific surface capacitance, based on its features with high tap density, a low S_{BET}, a high degree of graphitization, and a microporous characteristic.[20] However, there is a large space for enhancement in electrochemical performance of the polymer of PBPs (hereafter referred to as PPBP), especially in rate capability and cycling performance. Inspired by the fact that GO can tailor the growth of electroactive species to make them well-dispersed on the nanosheets,[1-3,17-19] we designed a strategy to produce RGO/PPBP nanocomposites with enhanced electrochemical performance for supercapacitors, as illustrated in Scheme 1. First, GO obtained through modified Hummers method[21] is dissolved in *N*-methyl-2-pyrrolidone (NMP) solution by ultrasonic treatment, followed by cooling the NMP solution to 0 °C. Then, newly-formed PBP ethanol solution is mixed with the NMP solution. The mixture is vigorously stirred for 2 h under Ar atmosphere. During the agitation process, GO sheets anchor PBP molecules through hydrogen bonding in the form of O–H···N or O···H–N (Scheme 1a). This is based on the facts that PBPs contain amino groups and GO is wealthy in oxygen-containing functional groups such as hydroxyl, carbonyl, carboxyl, and ether linkage.[2,16] Subsequently, the mixture is subjected to a microwave-assisted solvothermal process, followed by annealing the resulting precipitate at 500 °C under Ar atmosphere to produce GRO/PPBP nanocomposites. During microwave irradiation, PPBP is formed through thermal condensation of PBPs,[20] because halogenated pyrroles are not stable even at room temperature.[22] Meanwhile, GO is reduced to RGO in a microwave-assisted solvothermal system,[23] leading to the formation of RGO/PPBP. Moreover, PPBP can combine with RGO through covalent C–N bonding, accompanying with release of pore-making agents such as H_2O, CO, and CO_2 etc., during the microwave irradiation and anneal treatment (Scheme 1b). The anneal treatment at 500 °C is to optimize the electrochemical performance of the nanocomposites for supercapacitors, based on the result that PPBP obtained after anneal treatment at 500 °C for 12 h exhibits the optimum electrochemical properties.[20] As expected, the resulting RGO/PPBP nanocomposites exhibit enhanced electrochemical performance, compared with individual RGO,[4-8] graphene,[23,24] PPBP,[20] and many other carbon-based composites using graphene or RGO as the matrix in recent reports.[25-32]

2. Experimental section

2.1 Preparation of RGO/PPBP Nanocomposites

GO was prepared by a modified Hummers method,[21] and PBPs were synthesized through electrophilic bromination of pyrrole with bromine (Br_2) in absolute ethanol.[20] Detailed synthetic procedures with respect to GO and PBPs were provided in Electronic Supplementary Information (ESI). In a typical synthetic procedure for preparation of RGO/PPBP nanocomposites, 40 mg of GO were dissolved into 60 mL of NMP by ultrasonic treatment for 0.5 h, followed by cooling the NMP solution in a low-temperature reaction bath with temperature kept at 0 °C. Then, quantitative newly-formed PBP ethanol solution was mixed with the NMP solution. The mixture was vigorously stirred for 2 h under Ar atmosphere, followed by a microwave-assisted heat treatment at 180 °C for 0.5 h. The microwave power was set at 200 W. The resulting precipitate was collected by filtration, dried in a vacuum oven, and finally annealed at 500 °C for 12 h under Ar atmosphere

to produce RGO/PPBP-*n* samples, where *n* denotes the mass ratio of PPBP to RGO. For example, to obtain RGO/PPBP-1 sample, 2.6 mL of newly-formed PBP ethanol solution was mixed with the NMP solution containing 40 mg of GO. For comparison, individual PPBP and RGO were also prepared under otherwise identical conditions.

2.2 Characterization

X-ray diffraction (XRD) patterns were recorded on a Bruker D8 Advance diffractometer with Cu Kα radiation (λ = 1.5406 Å). Raman spectra were collected at room temperature on a Renishaw inVia plus laser Raman spectrometer with a 514 nm Ar^+ ion laser. Elemental analysis was performed on an Elementar Analysensysteme Vario EL III element analyzer. Scanning electron microscopy (SEM) images and energy-dispersive spectroscopy (EDS) mapping images were taken on a Hitachi S-4800 field-emission scanning electron microscope. Transmission electron microscopy (TEM) images were taken on a Philips Tecnai Twin-20U high-resolution transmission electron microscope, operating at an accelerating voltage of 200 kV. Scanning probe microscopy (SPM) images were taken on a Multimode 8 Nanoscope V system scanning probe microscope. Fourier transform infrared (FT-IR) spectra were collected on a Shimadzu IRPrestige-21 infrared spectrometer using pressed KBr discs. The FT-IR spectra were recorded with resolution of 4 cm^{-1} over the range of 4000–400 cm^{-1}. X-ray photoelectron spectroscopy (XPS) measurements were performed on a Thermo Fisher Scientific ESCALAB 250 X-ray photoelectron spectrometer, using monochromatic Al Kα radiation (1486.6 eV). To record C1s, N1s, and O1s high-resolution spectra, pass energy of 50 eV and step size of 0.05 eV were adopted. Binding energies for the high-resolution spectra were calibrated by setting C1s at 284.8 eV.

Nitrogen adsorption/desorption isotherms were collected at 77.1 K using an America Micromeritics ASAP 2020 sorptometer. Before recording the nitrogen sorption isotherms, the samples were degassed at 250 °C for 6 h. The Brunauer–Emmett–Teller (BET) method was utilized to calculate the specific surface areas (S_{BET}). The PSD was determined according to BJH desorption dV/dlog(r) pore volume plot and Horvath-Kawazoe differential pore volume plot, respectively.

The conductivity of the samples were measured on a four probe resistivity tester (Guangzhou Four Probe Tech., China). Sample powders were separately mixed with polyvinylidene fluoride (PVDF) in a mass ratio of 9:1 and then subjected to a pressure of 20 MPa to produce discs for measurement because individual RGO/PPBP-*n* samples produced fragile discs unsuitable for measurement.

2.3 Fabrication of Supercapacitors and Electrochemical Tests

The electrochemical properties of the samples were characterized at room temperature with cyclic voltammetry (CV), galvanostatic charge/discharge (GCD), and electrochemical impedance spectroscopy (EIS) techniques, using a CHI 660E electrochemical workstation (Shanghai CH Instruments Co., China).

In a three-electrode system, a platinum sheet was used as the counter electrode, Hg/Hg_2SO_4 electrode as the reference electrode, and 1 mol L^{-1} H_2SO_4 aqueous solution as the electrolyte. The working electrode was prepared by blade-coating well-blended slurry onto a stainless steel cloth, which served as the current collector. The slurry consists of 80 wt.% active material, 10 wt.% Super-P (conducting carbon), and 10 wt.% PVDF in NMP. The as-made electrodes were dried in a vacuum oven at 80 °C for 12 h, and then subjected to double rolling to ensure close contact between the active material and the current collector. The mass of active material upon stainless steel cloth was 2–3 mg, and the coating area was 1 cm^2.

In a two-electrode system, two symmetrical electrodes were soaked with 1 mol L^{-1} H_2SO_4, separated by a sulfonation film (BH5510, Shenzhen Gebang Co., China), and then assembled into a layered structure and sandwiched between two polytetrafluoroethylene (PTFE) sheets with parafilm. The active material on each electrode was ca. 2 mg. The thickness of the electrode film lies in the range of 40–62 μm by SEM, which is larger than the recommended value of 15 μm for commercial supercapacitors (Figure S1, ESI).[33]

CV and GCD curves were collected at –0.7–0.55 V vs. Hg/Hg_2SO_4 in a three-electrode mode and at 0–1 V in a two-electrode mode by varying scan rate from 1 to 200 mV s^{-1} and current density from 0.1 to 20 A g^{-1}, respectively. Alternating current (AC) EIS spectra were collected in a frequency range of 10^{-2}–10^5 Hz at the open circuit voltage with AC amplitude of 5 mV.

For three-electrode cells, gravimetric capacitance (C_g) derived from galvanostatic discharge curves was calculated from eq 1, represented as[4]

$$C_g = \frac{I\Delta t}{m\Delta V} \quad (1)$$

where C_g is the gravimetric capacitance (farad per gram), I the constant discharge current (ampere), Δt the discharge time (second), ΔV the voltage window (volts), and m the mass of active material on the working electrode (gram).

In a two-electrode system, the capacitance for a single electrode (C_{single}) was calculated according to eq 2, represented as[12,16]

$$C_{single} = \frac{4I\Delta t}{m\Delta V} \quad (2)$$

where m is the total mass of active material on the two electrodes (gram). The capacitance for the measured supercapacitor cell (C_{cell}) was calculated from eq 3, represented as[20]

$$C_{cell} = \frac{I\Delta t}{m\Delta V} \quad (3)$$

where m is the total mass of active material on the two electrodes (gram).

C_g derived from cyclic voltammograms was calculated from eq 4, represented as[24]

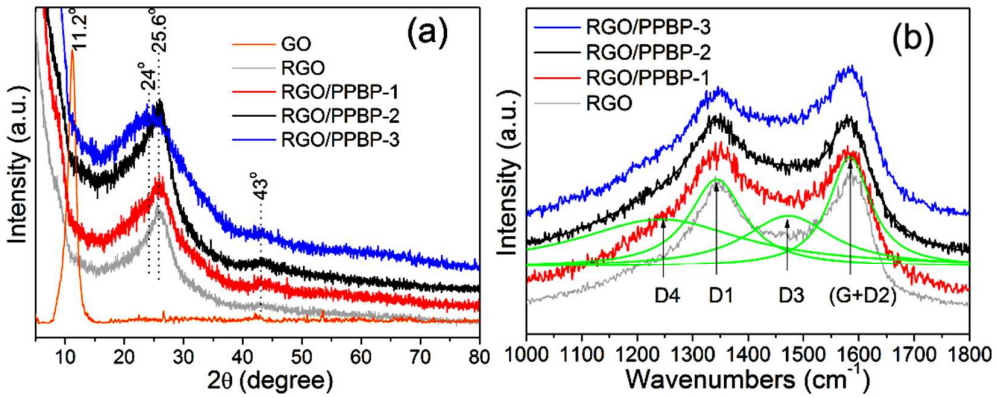

Figure 1. (a) XRD spectra and (b) Raman spectra of the samples.

$$C_g = \frac{1}{mv(V_b - V_a)} \int_{V_a}^{V_b} I dV \quad (4)$$

where m is the mass of active material on the working electrode (gram), v the scan rate (volts per second), I the discharge current (ampere), and V_b and V_a are the high and low voltage limit of the CV curves (volts).

The energy density (E) and power density (P) of the supercapacitor cell were estimated according to eqs 5 and 6, respectively, represented as[26]

$$E = \frac{C_{cell} \Delta V^2}{2} \quad (5)$$

$$P = \frac{E}{\Delta t} \quad (6)$$

where ΔV is the cell-operation voltage window (volts) and Δt the discharge time (second).

3. Results and discussion

3.1 Structure, Composition, and Morphology

Figure 1a shows the XRD spectra of the samples. The GO spectrum exhibits a strong peak at 11.2°, corresponding to the (002) plane with d-spacing of ca. 0.79 nm for GO.[5,7,12,24] It should be pointed out that the interlayer distance of GO is solvation-dependent because oxygen-containing solvent can function as an intercalation species due to the strong interaction between solvent molecules and oxygen-containing functional groups of GO.[12,24] After thermal reduction, the peak characteristic of GO disappears while a broad band peaked at 25.6° occurs corresponding to the (002) plane with d-spacing of ca. 0.35 nm for RGO (Figure 1).[5] The decrease in d-spacing for RGO is due to the removal of solvent and oxygen-containing functional groups.[24]

For the composite samples, the broad peak characteristic of the (002) plane of graphitic carbon is centered at 24–25.6°. The left shift in position of the broad peak with increasing d-spacing arises from two reasons. One reason is that the grafting of PPBP onto RGO suppresses restacking of RGO, and the other is attributed to turbostratic interlayer stacking of PPBP which is dominant in RGO/PPBP-3.[20] Also, a weak and broad peak characteristic of the (100) plane of graphitic carbon can be discerned at 43°. This result implies that the degree of graphitization for the composite samples can be improved by integrating PPBP with RGO, compared with individual RGO.

Figure 1b shows the Raman spectra of the samples. For each spectrum, there are two broad peaks centered around 1347 and 1583 cm^{-1}, which can be fitted into four or five bands through Gaussian/Lorentzian functions to provide more structural information (Table S1, ESI).[20,34] Taking RGO/PPBP-2 spectrum as an example, the two peaks can be fitted by Lorentzian function into four bands at 1243, 1344, 1473, and 1584 cm^{-1}, corresponding separately to disordered graphitic lattice (D4, 1243 cm^{-1}, 36.4% in total peak areas; D1, 1344 cm^{-1}, 22.0%), amorphous carbon (D3, 1473 cm^{-1}, 20.7%), and ordered graphitic lattice (G + D2, 1584 cm^{-1}, 20.9%). Usually, the intensity ratio of I_D/I_G is considered a measure of the degree of graphitization in partially graphitic carbons, and the I_D/I_G value decreases as the sp^2 domain size increases.[35] In the present case, we use $I_{D1}/I_{(G+D2)}$ to reflect the degree of graphitization of the samples (Table 1). It is found that the $I_{D1}/I_{(G+D2)}$ value for each composite sample is lower than that for individual RGO, and slightly decreases as the PPBP content increases. This result is indicative of a relatively higher degree of graphitization for the composite samples compared with that for individual RGO, in accordance with the XRD result. A relatively higher degree of graphitization with respect to RGO/PPBP is beneficial for improvement in electronic conductivity, which plays a crucial role in enhanced rate capability However, the conductivity of the samples decreases as the mass ratio of PPBP/RGO increases (Table 1). This is due to the bad contact between PPBP granules, in which RGO is coated.

The surface physics and chemistry of the samples were examined by the FT-IR and XPS techniques. Figure 2a shows the FT-IR spectra of the samples. The peaks in GO spectrum correspond separately to the ν(O–H) stretching vibration (3427 cm^{-1}), ν(C=O) stretching vibration (1710 cm^{-1}), δ(O–H) bending and ν(C=C) stretching

Table 1. Physicochemical properties of the samples.

sample	N content (at.%)		$I_{D1}/I_{(G+D2)}$	conductivity (S m^{-1})	BET analysis	
	CHN	XPS			S_{BET}	S_{micro}/S_{BET}
RGO/PPBP-1	5.57	9.06	0.798	43.3	378.4	–
RGO/PPBP-2	7.63	9.66	0.797	10.8	390.6	44.6%
RGO/PPBP-3	8.80	11.66	0.783	4.2	259.6	40.1%
RGO	–	–	0.866	357.1	173.1	–

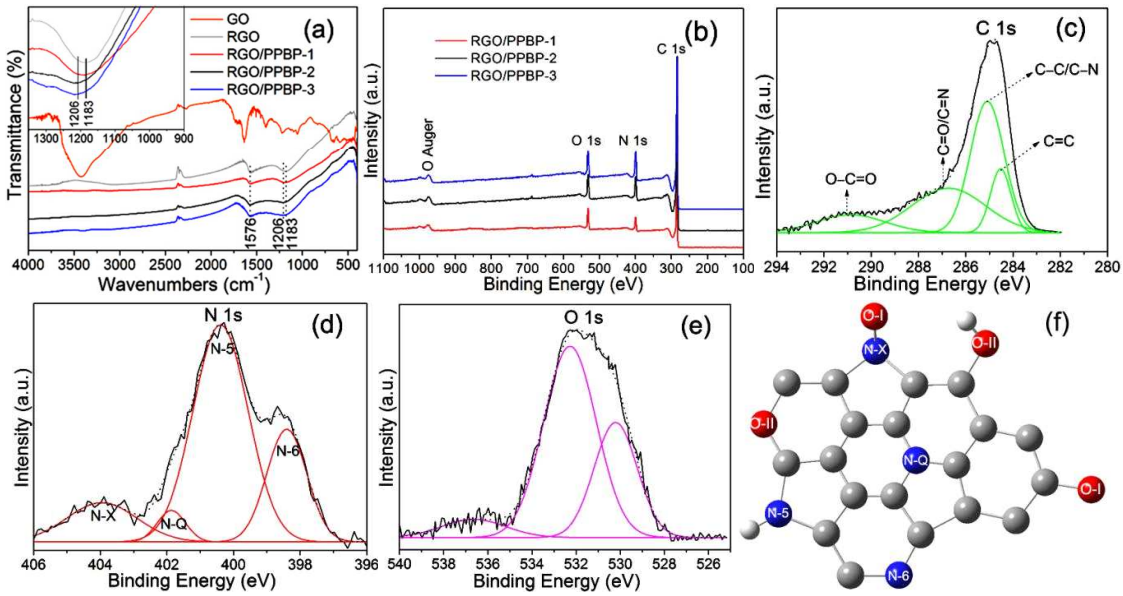

Figure 2. (a) FT-IR spectra; (b) XPS survey spectra; (c) C 1s for GRO/PPBP-2; (d) N 1s for GRO/PPBP-2; (e) O 1s for GRO/PPBP-2; (f) Illustration of different N and O components in PPBP.

vibrations (1632 cm^{-1}), γ(O–H) deforming vibration (1398 cm^{-1}), and ν(C–O)/ν(C–O–C) stretching vibrations (1219, 1091, 1054, 980, and 830 cm^{-1}),[7,25,29] indicating a wealth of oxygen-containing functional groups upon the GO sheets. However, there are mainly two broad bands centered at 1567 and 1183 cm^{-1} in RGO spectrum, corresponding separately to the ν(C=C) and ν(C–OH)/ν(C–O–C) stretching vibrations.[25] This result reveals that oxygen-containing functional groups still remains upon the carbon network after thermal reduction of GO at 500 °C for 12 h under Ar atmosphere, producing a RGO sample. The red shift in peak position of ν(C=C) for RGO compared with that for GO is due to the removal of oxygen-containing groups linked with sp^2-hybridized carbon. The RGO/PPBP spectra are similar to but not identical with the RGO spectrum, lying in that the band peaked at 1183 cm^{-1} for RGO blue-shifts to 1206 cm^{-1} for RGO/PPBP-3 (Figure 2a, inset). This is due to the existence of C=N and C–N bonds in the composite samples. Therefore, the two broad bands peaked at 1576 and 1183–1206 cm^{-1} are separately assigned to ν(C=C)/ν(C=N) and ν(C–O)/ν(C–N) stretching vibrations.

The existence of elemental N and O in the composite samples is confirmed by the XPS survey spectra (Figure 2b). The atomic percentage of N derived from the XPS data increases as the mass ratio of PPBP/RGO increases, in accordance with the CHN elemental analysis (Table 1). For N- and/or O-containing carbon-based materials, the electrochemical performance is highly dependent on the component ratio of heteroatoms.[20,36] In the present case, the components of C, N, and O are resolved by deconvolution of the high-resolution C1s, N1s, and O1s spectra (Figure 2c–e), and listed in Table S2 (ESI). Taking RGO/PPBP-2 as an example, the peaks at 284.5, 285.1, 286.7, and 290.9 eV correspond separately to sp^2-hybridized C=C (12.8%, in total area), sp^3-hybridized C–C (43.3%), C–O/C–N (32.0%), and O–C=O (11.9%) component (Figure 2c, green lines).[16,24,36] The low percentage of C=C (12.8%) is indicative of a highly functionalized surface. The fitted N1s spectrum exhibits four components at 398.4, 400.4, 401.9, and 403.9 eV (Figure 2d, red lines), corresponding separately to pyridinic N (N-6, 22.4%), pyrrolic/pyridone N (N-5, 59.5%), quaternary N (N-Q, 4.4%), and N-oxides (N-X, 13.7%).[16,20,37] It is well accepted that N-5 and N-6 have a high binding ability with electrolyte cations and N-Q improves the electronic conductivity of the material.[37,38] Therefore, high capacitive and rate capabilities are expected with respected to the N-containing composite samples. For the O1s spectrum, three components resolved by Gaussian fitting are centered at

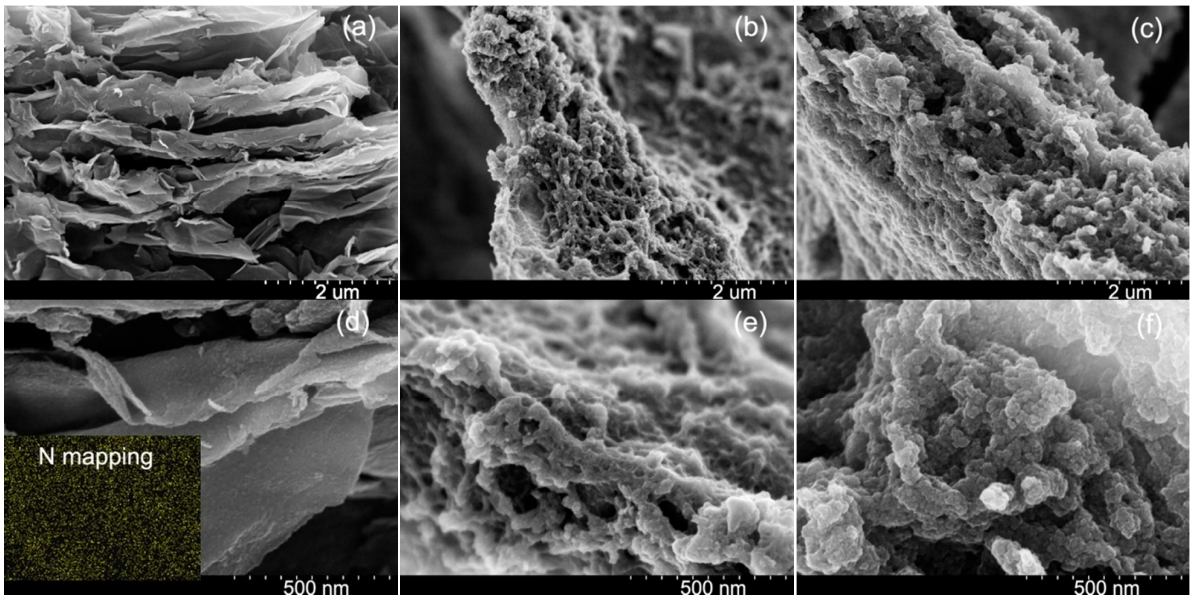

Figure 3. SEM images of the samples: (a,d) RGO/PPBP-1; (b,e) RGO/PPBP-2; (c,f) RGO/PPBP-3. d, e, and f are the high-magnification images corresponding separately to a, b, and c.

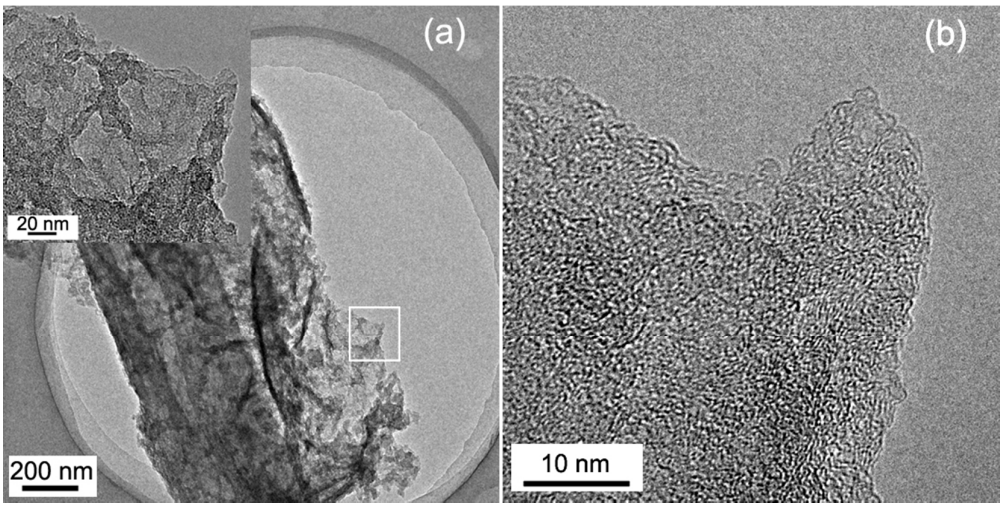

Figure 4. TEM images of RGO/PPBP-2: (a) low magnification; (b and inset in a) high-resolution images corresponding to the squared area in a.

530.2, 532.3, and 536.6 eV (Figure 2e, magenta lines), corresponding to C=O/C–N=O (O-I, 30.6%), C–OH/C–O–C (O-II, 62.2%), and chemisorbed oxygen and/or water (O-III, 7.2%), respectively.[37] The relatively higher percentage of C–O/C–N species revealed by the C1s and O1s spectra is consistent with the FT-IR result (Figure 2a). As demonstrated in literature,[36] O-I species contributes positively to reversible pseudocapacitance while O-II and O-III species offer irreversible pseudocapacitance for the oxygen-containing materials. Considering that RGO is coated by PPBP, the detected N and O in the XPS spectra mainly arise from the surface of PPBP. The components of N and O species in PPBP are illustrated in Figure 2f.

Figure 3 shows the SEM images of the samples. Compared with those of RGO (Figure S2a,b), the images of the composite samples exhibit rougher surfaces. For RGO/PPBP-1 (Figure 3a,d), the sample well retains the sheet morphology of RGO. It is worth noting that the both sides of an exfoliated RGO nanosheet are coated by a thin film of PPBP. This is confirmed by the SPM images of RGO/PPBP-2 (Figure S3, ESI) and the N-mapping image of RGO/PPBP-1 with homogeneous nitrogen distribution (Figure 2d, inset). As the mass ratio of PPBP/RGO increases to 2, the PPBP coating grows into a 2D network structure (Figure 3b,e) with thickness ranging from 1 to 6 nm (Figure S3, ESI). Further increase in the mass ratio of PPBP/RGO to 3 results in a featureless PPBP coating constituted by aggregated nanoparticles (Figure 3c,f), a situation that is similar to the growth of individual PPBP during thermal treatment (Figure S2c,d).

The network structure of RGO/PPBP-2 is also confirmed by the TEM images (Figure 4). The nanosheet with corrugated structure can be clearly observed in Figure 4a. Further

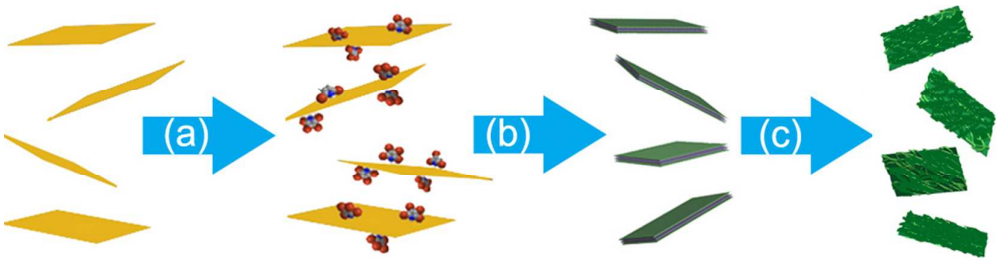

Scheme 2. Proposed formation mechanism of RGO/PPBP nanosheet with network structure: (a) PBPs combine with GO (yellow) through hydrogen bonding; (b) PPBP (dark green) grows on the both sides of RGO (gray); (c) formation of network-structured RGO/PPBP.

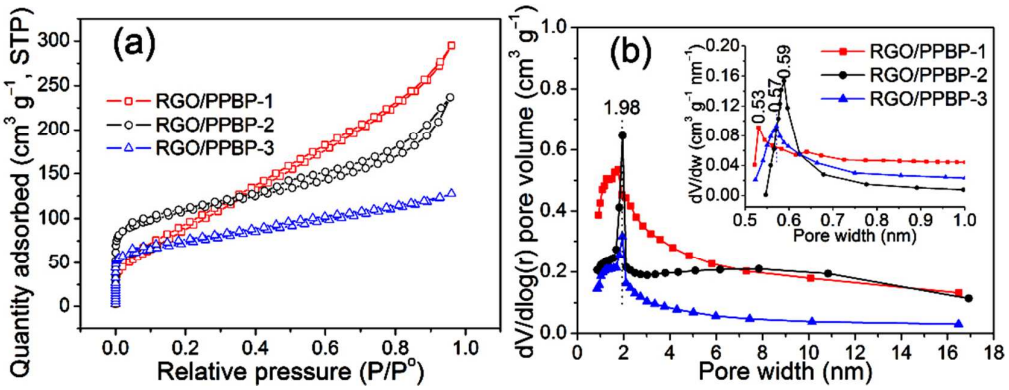

Figure 5. (a) Nitrogen sorption isotherms of the samples; (b) PSD plots of the samples.

examination shows the RGO nanosheet is coated by a 2D network-structured PPBP film, which can be discerned by the discrepancy in contrast of the image (Figure 4a, inset). High-resolution image reveals a partially graphitic PPBP film upon RGO (Figure 4b), in concert with the Raman result (Figure 1b).

3.2 Formation Mechanism

In fact, PPBP-coated RGO is formed during the microwave-assisted solvothermal process. As mentioned before, PBPs with amino groups combine with GO wealthy in oxygen-containing groups through hydrogen bonding during the mixing process (Schemes 1a and 2a). Under microwave irradiation, GO is reduced into RGO and PBPs polymerize into PPBP film on the both sides of RGO through self-propagation condensation (Scheme 2b and Figure 3d),[39] accompanying with release of Br_2 and HBr. The combination of RGO with PPBP is probably in the form of C–N bonding by releasing H_2O, CO, and CO_2 (Scheme 1b). The formation of RGO is due to the reducibility of NMP under microwave irradiation. As reported in literature,[40] NMP can be easily oxidized into *N*-methylsuccinimide (NMS) under thermal treatment in air. Therefore, NMP has been utilized as both solvent and an oxygen-scavenger for GO to produce exfoliated RGO at the boiling temperature.[41] To verify the role of NMP in the microwave-assisted solvothermal reduction process, individual NMP was subjected to microwave irradiation (200 W) at 180 °C for 30 min. It is found that the uncolored solvent slowly turns brown during irradiation. Using the gas chromatography/mass spectrometry (GC/MS) technique, the resulting products in NMP are determined to be pyrrolidone (**1**, *M*w 85), 1-methyl-1H-pyrrol-2(5H)-one (**2**, *M*w 97), and NMS (**3**, *M*w 113) (Table S3, ESI). This result indicates that the reducibility of NMP arises from both the oxygen-scavenging property and the produced H_2 during the formation of compound **2**. On the other hand, as a by-product released from both electrophilic substitution of pyrrole with Br_2 and polymerization of PBPs, HBr can function as a reducing agent to reduce GO into RGO.[42] With increasing the volume of PBP ethanol solution in reaction medium, the PPBP coating grows into a network structure (Scheme 2c and Figure 3b). This is attributed to the corrugated RGO matrix and the anisotropic growth behavior of the polymer.[20] In the case of a large amount of PBPs in reaction medium, except a portion of PPBP grows on the surface of the matrix to form RGO/PPBP nanosheet, considerable portion of PPBP individually nucleates in solution. These individually nucleated PPBP nanoparticles agglomerate and adhere to the surface of the newly-formed RGO/PPBP nanosheet through van der Waals interactions, leading to the formation of RGO/PPBP composite with featureless characteristic (Figure 3c).

3.3 BET Analysis

The S_{BET} and PSD of the samples have also been evaluated because they are closely related to the electrochemical performance of electrode materials. Detailed data from BET analysis are provided in Table S4 (ESI). Compared with that for RGO/PPBP-1, the nitrogen sorption isotherms for RGO/PPBP-2 and RGO/PPBP-3 (Figure 5a) exhibit an apparent microporous characteristic reflected by the type-I

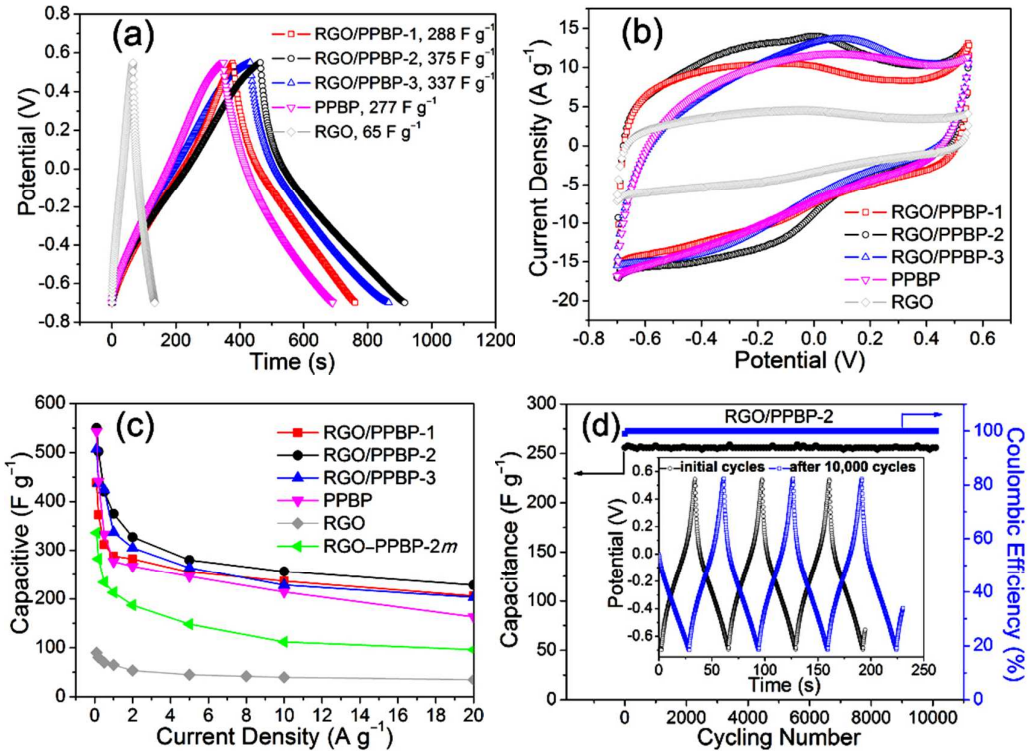

Figure 6. Electrochemical performance of the samples tested in a three-electrode mode: (a) Galvanostatic charge/discharge curves at 1 A g^{-1}; (b) cyclic voltammograms at 50 mV s^{-1}; (c) plots of C_g as a function of current density; (d) cycling performance at 10 A g^{-1}; inset is the GCD curves at the initial stage and after 10,000 cycles.

sorption curves with abrupt adsorption plateau at the low relative-pressure region ($P/P^o < 0.4$).[43] Also, the observed hysteresis loops at high relative-pressure region ($P/P^o > 0.4$) reveal the coexistence of meso- and macropores.[12,27] The micropores are mainly caused by the small molecules (e.g. HBr, Br_2, H_2O, CO, CO_2, NH_4Br, and C_2H_xN) released during the microwave irradiation and thermal treatment.[20] The mesopores are attributed to stacking of both RGO/PPBP nanosheets and PPBP nanoparticles. Both micro- and mesopores can function as electrolyte container allowing quick ion motion during charge/discharge processes to improve rate performance of the electrode materials.[44] Compared with that for individual RGO, the S_{BET} for RGO/PPBP is greatly improved (Table 1). This result indicates that combination of PPBP with RGO can prevent restacking of RGO sheets, consolidating the suggestion that PPBP grows on the both sides of RGO (Scheme 2b). Compared with that for RGO/PPBP-1 and RGO/PPBP-2, the S_{BET} for RGO/PPBP-3 is decreased, due to the agglomeration of PPBP granules.

Figure 5b shows the PSD plot of RGO/PPBP samples, where micropores and mesopores coexist and micropores with pore width centered at 1.74–1.98 nm are abundant. The microporous characteristic of the samples is further reflected by the Horvath-Kawazoe differential pore volume plot (Figure 5b, inset), where subnanopores with pore width centered at 0.53, 0.59, and 0.57 nm dominate the subnanopores in RGO/PPBP-1, RGO/PPBP-2, and RGO/PPBP-3, respectively. As demonstrated in literature,[45] electrode materials with relatively high S_{BET} and abundant subnanopores exhibit high electrochemical double layer capacitance (EDLC) according to equation represented as

$$C = \frac{\varepsilon_r \varepsilon_0 A}{d} \quad (7)$$

where ε_r is the electrolyte dielectric constant, ε_0 is the dielectric constant of the vacuum, A is the electrode surface area, and d the charge separation distance.

On the basis of the above analysis, we conclude that RGO/PPBP nanocomposites can be obtained through a microwave-assisted solvothermal approach followed by anneal treatment. The composites are featured with high nitrogen content, enhanced degree of graphitization, improved S_{BET} and abundant micropores, and a tunable hierarchical structure. These features ensure superior electrochemical performance of the samples when tested in the role of electrode materials for supercapacitors.

3.4 Electrochemical Properties

Figure 6a shows the typical GCD curves of the samples in three-electrode cells at a current density of 1 A g^{-1}. It is found that RGO/PPBP electrodes exhibit longer discharge times than individual PPBP and RGO. This result indicates superior

electrochemical performance of the composite samples in accordance with the result of CV measurements (Figure 6b). The capacitive performance of the samples was also examined as a function of the current density (Figure 6c). Although individual PPBP exhibits a comparable C_g value (543 F g^{-1}) to that of RGO/PPBP (438, 550, 507 F g^{-1}) at 0.1 A g^{-1}, its rate capability is inferior to that for the composite samples. For example, the C_g values for RGO/PPBP-1, RGO/PPBP-2, RGO/PPBP-3, and PPBP are 288, 375, 337, and 277 F g^{-1}, respectively, as the current density increases to 1 A g^{-1}. In the case of individual RGO, it exhibits good rate capability but bad capacitive performance. As a result, the RGO/PPBP nanocomposites exhibit enhanced capacitive and rate performance compared with individual PPBP and RGO. This indicates a synergistic effect between PPBP and RGO, where PPBP anchoring on RGO suppresses agglomeration and restacking of RGO, thereby resulting in an increased available surface area for RGO and, hence, enhanced EDLC. On the other hand, GO serves as a support to anchor PBPs so that PPBP nucleates and grows with good dispersion and tunable structure on the both sides of RGO, maximizing the EDLC and pseudocapacitance contributed from PPBP. In other words, the integrated RGO/PPBP structure with developed electron conductive network and shortened ion transport paths is responsible for the enhanced capacitance. We infer that the integrated RGO/PPBP structure is through the covalent C–N bonding between the two components. To confirm this inference, individual RGO and PPBP were mechanically blended to form a RGO–PPBP mixture with mass ratio of PPBP/RGO equaling 2, hereafter referred to as RGO–PPBP-2*m*. The electrochemical performance of RGO–PPBP-2*m* was also examined as shown in Figure 6c. It is apparent that RGO–PPBP-2*m* exhibits much inferior performance to RGO/PPBP, counter-evidencing a strong combination rather a simple blending between the two components.

The inflections at 0–0.1 V in discharge curves (Figure 6a) are attributed to the pseudocapacitive contribution from heteroatom functional groups,[46] corresponding well to the Faradaic humps in the anodic sweeps of CV with quasi-rectangular shape (Figure 6b). Among the RGO/PPBP electrodes, RGO/PPBP-2 exhibits the highest electrochemical (Figure 6c). In view of the similar degree of graphitization (Table 1) and nitrogen component distribution (Table S2, ESI) among RGO/PPBP samples, the superior electrochemical performance of RGO/PPBP-2 is attributed to its corrugated 2D network structure and relatively higher S_{BET} and S_{micro}/S_{BET}. The cycling stability of the electrodes was tested at 10 A g^{-1} in a three-electrode mode. After 10,000 cycles, the RGO/PPBP electrodes exhibit high C_g and capacitance retention (Table 2), especially for RGO/PPBP-2 (Figure 6d) whose GCD curves after 10,000 cycles resemble those of the initial cycles (Figure 6d, inset). Also, the Coulombic efficiency is 100% after the first cycle. This result indicates excellent capacitive reversibility, rate capability, and cycling performance of RGO/PPBP-2.

To evaluate possible practical application in supercapacitors, the electrochemical performance of RGO/PPBP-2‖RGO/PPBP-2 supercapacitor cell was further tested, using 1 mol L^{-1} H_2SO_4 as the electrolyte. The discharge curves are almost symmetric with the charge curves at the current density range of 0.1–5 A g^{-1} (Figure 7a) , indicating a high capacitive reversibility.[12] The quasi-rectangular shape of the CV (Figure 7b) at the scan rate range of 1–100 mV s^{-1} reflects

Table 2. Comparison in the electrochemical performance of the samples with other advanced electrode materials in recent reports.

sample	initial C_g (F g^{-1})	current density/ cycle number	electrolyte	C_g retention (%)	E (Wh kg^{-1})/ P (kW kg^{-1})	refs.
RGO/PPBP-1[a]	232	10 A g^{-1}/10,000	1 M H_2SO_4	99.6	–	this work
RGO/PPBP-2[a]	256	10 A g^{-1}/10,000	1 M H_2SO_4	99.2	–	this work
RGO/PPBP-2[b]	272	5 A g^{-1}/10,000	1 M H_2SO_4	91.9	9.4/2.5	this work
RGO/PPBP-3[a]	246	10 A g^{-1}/10,000	1 M H_2SO_4	91.9	–	this work
PPBP[a]	216	10 A g^{-1}/10,000	1 M H_2SO_4	88.9	–	this work
RGO[a]	40	10 A g^{-1}/10,000	1 M H_2SO_4	120	–	this work
RGO[b]	188*	0.5 A g^{-1}/10,000	6 M NaOH	97	–	7
carbon/graphene[b]	238.8	2.5 A g^{-1}/3000	1 M H_2SO_4	94	–	25
nitrogen-doped graphene[a]	197	0.5 A g^{-1}/5000	6 M NaOH	98	–	26
N-carbon nanorods/graphene[a]	201	1 A g^{-1}/3000	6 M NaOH	98.7	–	27
graphene/PPy areogel[a]	138	10 A g^{-1}/2000	1 M H_2SO_4	93	–	28
NH_2-RGO/PANI[b]	345	2 A g^{-1}/1000	1 M H_2SO_4	85	9.6/0.8*	29
sulfonated graphene/PPy[b]	360	1 A g^{-1}/500	1 M H_2SO_4	90	–	30
Graphene/carbon nanohorn[b]	166	10 A g^{-1}/1000	1 M NaOH	99	–	31

a. C_g measured in a three-electrode mode; b. C_g measured in a two-electrode mode.* Values estimated from the information given in references.

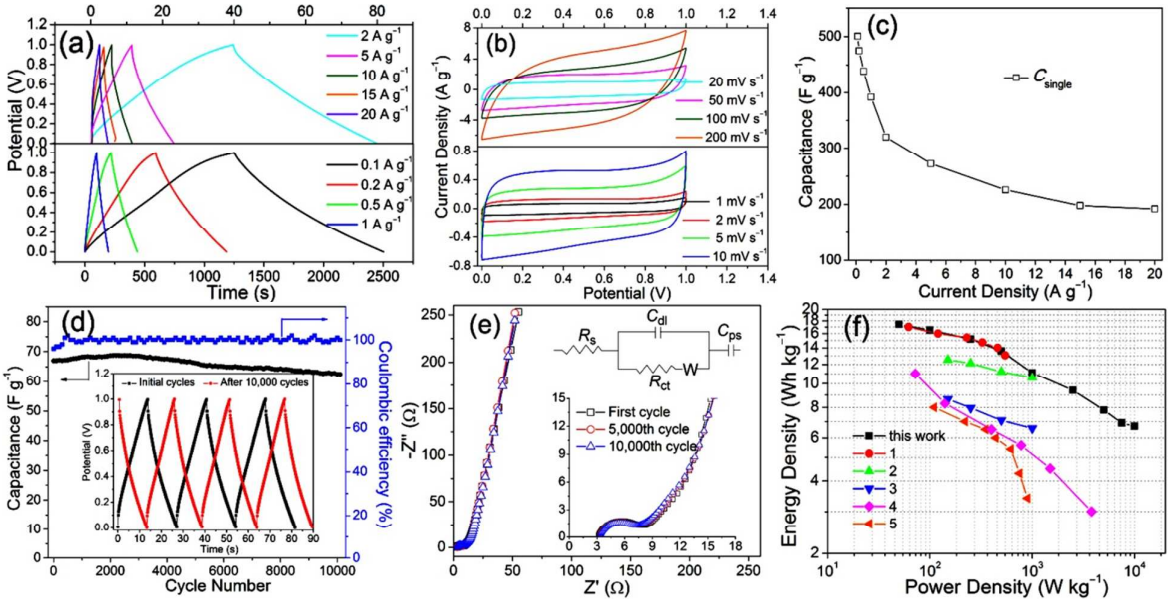

Figure 7. Electrochemical performance of RGO/PPBP-2||RGO/PPBP-2 supercapacitor cell: (a) Galvanostatic charge/discharge curves; (b) cyclic voltammograms; (c) plot of C_{single} as a function of the current density; (d) cycling performance at 5 A g^{-1}; inset is the GCD curves at the initial stage and after 10,000 cycles; (e) Nyquist plots and equivalent circuit; (f) Ragone plots (1. N-RGO/PANI,[48] 2. RGO/PANI,[32] 3. RGO/PPy,[32] 4.MnO_2 nanowire/Graphene,[49] 5. 3D N,B-codoped graphene.[50])

a typical capacitive behavior due to the simultaneous EDLC and pseudocapacitance.[25] Moreover, the CV retains the quasi-rectangular shape as the scan rate increases to 200 mV s^{-1}, indicating a good high-rate capability of the cell. The plot of capacitance versus current density for a single electrode (C_{single}) exhibits C_{single} values of 500.4, 474.8, 438.8, 392, 320, 272, 226, and 192 F g^{-1} at 0.1, 0.2, 0.5, 1, 2, 5, 10, and 20 A g^{-1}, respectively (Figure 7c). Compared with the three-electrode system, the decrease in C_{single} value measured by the two-electrode mode is attributed to the mass/charge transfer resistance caused by the separation film. The cycling stability of the cell was tested at 5 A g^{-1}, presenting a nearly 100% Coulombic efficiency and a capacitance retention of 91.9% after 10,000 cycles (Figure 7d). The high cycling stability of the cell can be reflected by GCD curves after 10,000 cycles, which are very similar to those of the initial cycles (Figure 7d, inset). Moreover, the cycling stability is confirmed by the Nyquist plots (Figure 7e), where the ohmic resistance of the electrodes (R_s), derived from the electrolyte and the contact between electrode and current collector, increases by only 0.12 and 0.14 Ω after 5,000th and 10,000th cycle, respectively. Also, the charge-transfer resistance (R_{ct}) and the Warburg-type resistance (W) exhibit nearly no change after 10,000 cycles. This result indicates the charge transportation has not been blocked during the cycling process, evidencing high structural stability of RGO/PPBP-2 whose structural deformation arising from PPBP component is alleviated by RGO due to the synergistic effect between the two components. Using Zsimpwin software, the impedance data are analyzed by fitting to an equivalent circuit consisting of R_s, R_{ct}, W, C_{dl}, and C_{ps} (Figure 7e, inset),[47] where C_{dl} and C_{ps} in the circuit represents EDLC and pseudocapacitance, respectively. The fitted impedance data match well with the experimental data (Figure S4 and Table S5, ESI).

The energy density and powder density of the cell are calculated according to eqs 5 and 6. The Ragone plot of the cell (Figure 7f) exhibits energy density values of 17.4, 16.5, 15.2, 13.6, 11.1, 9.4, 7.8 and 6.7 Wh kg^{-1} with corresponding power density of 0.05, 0.1, 0.25, 0.5, 1, 2.5, 5, and 10 kW kg^{-1}, indicating that relatively high energy density can be achieved without compromising the power density. Compared with the advanced electrode materials in recent reports (Table 2 and Figure 7f), our RGO/PPBP samples exhibit superior capacitive, rate, and/or cycling performance to RGO or graphene,[4-8,23,24] PPBP,[20] nitrogen-doped graphene,[26] spine-like carbon/graphene,[25] N-doped carbon nanorods/grahene,[27] graphene/polypyrrole (PPy) nanotubes aerogel,[28] NH_2-RGO/polyaniline (PANI),[29,48] sulfonated graphene/PPy,[30] nanoporous graphene/carbon nanohorn,[31] RGO/conducting polymers,[32] MnO_2 nanowire/graphene,[49] and N,B-codoped graphene.[50] This result enables the tested cell to stay at the high level for carbon-based supercapacitors with aqueous electrolyte (Figure 7f).

4. Conclusion

In summary, RGO/PPBP nanocomposites have been prepared by grafting PPBP onto RGO through a microwave-assisted solvothermal approach followed by anneal treatment. Also, the samples have been tested in the role of electrode materials for supercapacitors. The scientific significance of this research lies in: (1) grafting PPBP onto RGO not only suppresses

agglomeration and restacking of RGO but also tailor the growth of PPBP on RGO, producing a developed 2D network-structure beneficial for mass/charge transfer; (2) growth of PPBP on RGO offers an enhanced degree of graphitization for RGO/PPBP compared with that for individual RGO; (3) small molecules (e.g. Br_2, HBr, NH_4Br, H_2O, CO, CO_2) released during the polymerization of PBPs and formation of RGO/PPBP serve as pore-making agents, allowing RGO/PPBP to have abundant micropores coexisting with mesopores; (4) integrated RGO/PPBP structure can be tuned by varying the mass ratio of PPBP/RGO; (5) strong combination between RGO and PPBP through microwave irradiation in combination with anneal treatment ensures a synergistic effect between RGO and PPBP; and (6) superior capacitive, rate, and cycling performance as well as relatively wide potential window with respect to RGO/PPBP-2 result in high energy density/power density couples for symmetric RGO/PPBP-2‖RGO/PPBP-2 cell, presenting a promising candidate for carbon-based supercapacitors working with aqueous electrolyte. In addition, the RGO/PPBP samples have great potentials as electroactive materials in lithium-ion batteries, fuel batteries, and oxygen reduction reactions.

Acknowledgments

This research was financially supported by National Natural Science Foundation of China under Grant No. 51272143 and 51472278.

References

1 G. Yu, X. Xie, L. Pan, Z. Bao and Y. Cui, *Nano Energy*, 2013, **2**, 213–234.
2 M. Pumera, *Chem. Soc. Rev.*, 2010, **39**, 4146–4157.
3 Z. S. Wu, G. Zhou, L. C. Yin, W. Ren, F. Li and H. M. Cheng, *Nano Energy*, 2012, **1**, 107–131.
4 M. D. Stoller, S. Park, Y. Zhu, J. An and R. S. Ruoff, *Nano Lett.*, 2008, **8**, 3498–3502.
5 Y. Zhu, M. D. Stoller, W. Cai, A. Velamakanni, R. D. Piner, D. Chen and R. S. Ruoff, *ACS Nano*, 2010, **4**, 1227–1233.
6 C. Liu, Z. Yu, D. Neff, A. Zhamu and B. Z. Jang, *Nano Lett.*, 2010, **10**, 4863–4868.
7 A. M. Abdelkader, C. Vallés, A. J. Cooper, I. A. Kinloch and R. A. W. Dryfe, *ACS Nano*, 2014, **8**, 11225–11233.
8 Y. Lin, X. Han, C. J. Campbell, J.-W. Kim, B. Zhao, W. Luo, J. Dai, L. Hu and J. W. Connell, *Adv. Funct. Mater.*, 2015, **25**, 2920–2927.
9 Y. Zhu, S. Murali, M. D. Stoller, K. J. Ganesh, W. Cai, P. J. Ferreira, A. Pirkle, R. M. Wallace, K. A. Cychosz, M. Thomme, D. Su, E. A. Stach and R. S. Ruoff, *Science*, 2011, **332**, 1537–1541.
10 X. Yang, C. Cheng, Y. Wang, L. Qiu and D. Li, *Science*, 2013, **341**, 534–537.
11 X. Yang, J. Zhu, L. Qiu and D. Li, *Adv. Mater.*, 2011, **23**, 2833–2838.
12 Y. Yoon, K. Lee, C. Baik, H. Yoo, M. Min, Y. Park, S. M. Lee and H. Lee, *Adv. Mater.*, 2013, **25**, 4437–4444.
13 U. N. Maiti, J. Lim, K. E. Lee, W. J. Lee and S. O. Kim, *Adv. Mater.*, 2014, **26**, 615–619.
14 D. Y. Yeom, W. Jeon, N. D. Kha Tu, S. Y. Yeo, S. S. Lee, B. J. Sung, H. Chang, J. A. Lim and H. Kim, *Sci. Rep.*, 2015, DOI: 10.1038/srep09817.
15 J. Zhao, H. Lai, Z. Lyu, Y. Jiang, K. Xie, X. Wang, Q. Wu, L. Yang, Z. Jin, Y. Ma, J. Liu and Z. Hu, *Adv. Mater.*, 2015, **27**, 3541–3545.
16 P. Chen, J. J. Yang, S. S. Li, Z. Wang, T. Y. Xiao, Y. H. Qian and S. H. Yu, *Nano Energy*, 2013, **2**, 249–256.
17 F. Bonaccorso, L. Colombo, G. Yu, M. Stoller, V. Tozzini, A. C. Ferrari and R. S. Ruoff, *Science*, 2015, **347**, DOI:10.1126/science.1246501.
18 R. Raccichini, A. Varzi, S. Passerini and B. Scrosati, *Nat. Mater.*, 2015, **14**, 271–279.
19 G. Xie, K. Zhang, B. Guo, Q. Liu, L. Fang and J. R. Gong, *Adv. Mater.*, 2013, **25**, 3820–3839.
20 S. Wang, L. Gai, J. Zhou, H. Jiang, Y. Sun and H. Zhang, *J. Phys. Chem. C*, 2015, **119**, 3881–3891.
21 W. S. Hummers and R. E. Offeman, *J. Am. Chem. Soc.*, 1958, **80**, 1339.
22 H. M. Gilow and D. E. Burton, *J. Org. Chem.*, 1981, **46**, 2221–2225.
23 Y. Zhu, S. Murali, M. D. Stoller, A. Velamakanni, R. D. Piner and R. S.Ruoff, *Carbon*, 2010, **48**, 2118–2122.
24 Z. Bo, X. Shuai, H. Yang, J. Qian, J. Chen, J. Yan and K. Cen, *Sci. Rep.*, 2014, DOI: 10.1038/srep04684.
25 S. H. Park, S. B. Yoon, H. K. Kim, J. T. Han, H. W. Park, J. Han, S. M. Yun, H. G. Jeong, K. C. Roh and K. B. Kim, *Sci. Rep.*, 2014, DOI: 10.1038/srep06118.
26 K. Wang, L. Li, T. Zhang and Z. Liu, *Energy*, 2014, **70**, 612–617.
27 H. S. Fan, H. Wang, N. Zhao, J. Xu and F. Pan, *Sci. Rep.*, 2014, DOI: 10.1038/srep07426.
28 S. Ye and J. Feng, *ACS Appl. Mater. Interfaces*, 2014, **6**, 9671−9679.
29 L. Lai, H. Yang, L. Wang, B. Kin Teh, J. Zhong, H. Chou, L. Chen, W. Chen, Z. Shen and R. S. Ruoff, *ACS Nano*, 2012, **6**, 5941–5951.
30 C. Bora and S. Dolui, *J. Phys. Chem. C*, 2014, **118**, 29688–29694.
31 K. P. Annamalai, J. Gao, L. Liu, J. Mei, W. Lau and Y. Tao, *J. Mater. Chem. A*, 2015, **3**, 11740–11744.
32 J. Zhang and X. S. Zhao, *J. Phys. Chem. C*, 2012, **116**, 5420–5426.
33 M. D. Stoller and R. S. Ruoff, *Energy Environ. Sci.*, 2010, **3**, 1294–1301.
34 A. Sadezky, H. Muckenhuber, H. Grothe, R. Niessner and U. Pöschl, *Carbon*, 2005, **43**, 1731–1742.
35 J. Kaufman, S. Metin and D. Saperstein, *Phys. Rev. B*, 1989, **39**, 13053–13060.
36 Y. Fang, B. Luo, Y. Jia, X. Li, B. Wang, Q. Song, F. Kang and L. Zhi, *Adv. Mater.*, 2012, **24**, 6348–6355.
37 M. Seredych, D. Hulicova-Jurcakova, G. Q. Lu and T. J. Bandosz, *Carbon*, 2008, **46**, 1475–1488.
38 F. Su, C. K. Poh, J. S. Chen, G. Xu, D. Wang, Q. Li, J. Lin and X. W. Lou, *Energy Envion. Sci.*, 2011, **4**, 717–724.
39 J. R. Holst and E. G. Gillan, *J. Am. Chem. Soc.*, 2008, **130**, 7373–7379.
40 C. M. White, P. C. Rohar, G. A. Veloski and R. R. Anderson, *Energy Fuels*, 1997, **11**, 1105–1106.
41 S. Dubin, S. Gilje, K. Wang, V. C. Tung, K. Cha, A. S. Hall, J. Farrar, R. Varshneya, Y. Yang and R. B. Kaner, *ACS Nano*, 2010, **4**, 3845–3852.
42 Y. Chen, X. Zhang, D. Zhang, P. Yu and Y. Ma, *Carbon*, 2011, **49**, 573–580.
43 D. C. Guo, J. Mi, G. P. Hao, W. Dong, G. Xiong, W. C. Li and A. H. Lu, *Energy Environ. Sci.*, 2013, **6**, 652–659.
44 Y. Zhao, B. Liu, L. Pan and G. Yu, *Energy Environ. Sci.*, 2013, **6**, 2856–2870.

45 J. Chmiola, G. Yushin, Y. Gogotsi, C. Portet, P. Simon and P. L. Taberna, *Science*, 2006, **313**, 1760–1763.
46 K. Yang, L. Peng, D. Shu, C. Lv, C. He and L. Long, *J. Power Sources*, 2013, **239**, 553–560.
47 S. K. Meher and G. R. Rao, *J. Phys. Chem. C*, 2011, **115**, 15646–15654.
48 K. Gopalakrishnan, S. Sultan, A. Govindaraj and C. N. R. Rao, *Nano Energy*, 2014, **12**, 52–58.
49 Z. S. Wu, W. Ren, D. W. Wang, F. Li, B. Liu and H. M. Cheng, *ACS Nano*, 2010, **4**, 5835–5842.
50 Z. S. Wu, A. Winter, L. Chen, Y. Sun, A. Turchanin, X. Feng and K. Müllen, *Adv. Mater.*, 2012, **25**, 5130–5135.

Graphical Abstract

An integrated structure has been designed by grafting polymer of polybromopyrroles (PPBP) onto reduced graphene oxide (RGO) to produce RGO/PPBP nanocomposites superior electrochemical performance for supercapacitors.